Cell Reports
Medicine

Article

Osteoclast-derived apoptotic bodies inhibit naive CD8$^+$ T cell activation via Siglec15, promoting breast cancer secondary metastasis

Graphical abstract

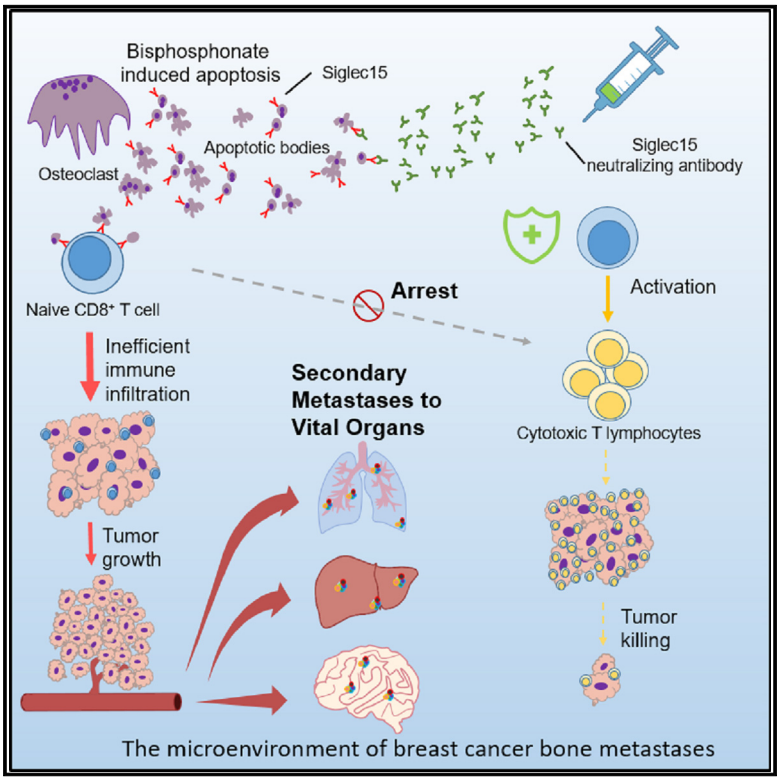

Highlights

- Osteoclast apoptotic bodies exhibit immunosuppressive effects in the bone-tumor niche
- Osteoclast apoptotic bodies suppress the activation of naive CD8$^+$ T cells via Siglec15
- Anti-Siglec15 therapy reduces secondary metastases of breast cancer bone metastasis
- Siglec15 is a common target for anti-resorption and immunotherapy in bone

Authors

Yutong Wu, Hongbo Ai, Yuhang Xi, ..., Jianzhong Xu, Fei Luo, Ce Dou

Correspondence

xujianzhong1962@163.com (J.X.), luofly1009@21cn.com (F.L.), lance.douce@gmail.com (C.D.)

In brief

Wu et al. discover that Siglec15 on osteoclast-derived apoptotic bodies binds to TLR2 on naive CD8$^+$ T cells, suppressing their function and promoting breast cancer cell spread from bone to distant organs. Anti-Siglec15 therapy in mice is bone protective, reduces secondary metastases, and improves survival in breast cancer bone metastasis.

Wu et al., 2023, Cell Reports Medicine *4*, 101165
September 19, 2023
https://doi.org/10.1016/j.xcrm.2023.101165

CellPress

Cell Reports Medicine

CellPress
OPEN ACCESS

Article

Osteoclast-derived apoptotic bodies inhibit naive CD8$^+$ T cell activation via Siglec15, promoting breast cancer secondary metastasis

Yutong Wu,[1,2] Hongbo Ai,[1,2] Yuhang Xi,[1] Jiulin Tan,[1] Ying Qu,[1] Jianzhong Xu,[1,*] Fei Luo,[1,*] and Ce Dou[1,3,*]
[1]Department of Orthopedics, Southwest Hospital, Third Military Medical University (Army Medical University), Chongqing 400038, China
[2]These authors contributed equally
[3]Lead contact
*Correspondence: xujianzhong1962@163.com (J.X.), luofly1009@21cn.com (F.L.), lance.douce@gmail.com (C.D.)
https://doi.org/10.1016/j.xcrm.2023.101165

SUMMARY

The bone microenvironment promotes cancer cell proliferation and dissemination. During periodic bone remodeling, osteoclasts undergo apoptosis, producing large numbers of apoptotic bodies (ABs). However, the biological role of osteoclast-derived ABs, which are residents of the bone-tumor niche, remains largely unknown. Here, we discover that AB-null MRL/lpr mice show resistance to breast cancer cell implantation, with more CD8$^+$ T cell infiltrations and a higher survival rate. We uncover that the membranous Siglec15 on osteoclast-derived ABs binds with sialylated Toll-like receptor 2 (TLR2) and blocks downstream co-stimulatory signaling, leading to the inhibition of naive CD8$^+$ T cell activation. In addition, our study shows that treatment with Siglec15 neutralizing antibodies significantly reduces the incidence of secondary metastases and improves the survival rate of mice with advanced breast cancer bone metastasis. Our findings reveal the immunosuppressive function of osteoclast-derived ABs in the bone-tumor niche and demonstrate the potential of Siglec15 as a common target for anti-resorption and immunotherapy.

INTRODUCTION

Bone is the most frequently affected organ and often the first site of breast cancer metastasis.[1] Recent studies have shown that the bone microenvironment facilitates further metastasis of breast cancer cells, leading to the establishment of multi-organ secondary metastases and catastrophic outcomes.[2] In the bone microenvironment (BME), metastases are driven by a vicious cycle between cancer cells and osteoclasts.[3] However, although targeting osteoclasts with bisphosphonates (BPs) can limit metastasis progression, it cannot extend overall survival.[4]

In bone remodeling, osteoclasts undergo apoptosis after the bone resorption phase, producing an extensive number of apoptotic bodies (ABs).[5] Contrary to the traditional view of ABs as "waste bags," we have previously shown that osteoclast-derived ABs are crucial in coupling bone resorption and formation.[6–8] Due to the lifetime periodic remodeling process, these osteoclast-derived ABs become a resident component of the BME. However, it remains completely unknown whether these osteoclast-derived ABs play a role in the bone-tumor niche.

CD8$^+$ T cell-mediated cytotoxicity is essential for breast cancer immunity,[9,10] and tumor CD8$^+$ T cell infiltration is associated with a reduced risk of death in patients with breast cancer.[11–13] Despite the effectiveness of cancer immunotherapy in a subset of cancers, in patients with programmed death ligand 1 (PD-L1)$^+$ advanced breast cancer, PD1 blockade only shows an overall response rate of 18.5%.[14] Recent studies have shown that Siglec15, as an immunosuppressive molecule largely operating in the tumor microenvironment, is non-redundant to the PD1 pathway.[15]

We have previously demonstrated that osteoclast maturation is dependent on Siglec15-mediated cell recognition.[16] Here, we showed that Siglec15 is mostly enriched in osteoclast-derived ABs. We assume that the increase of osteoclast-derived ABs in the bone-tumor niche, caused by BP-induced cell apoptosis, might attribute to the limitations of BP-based adjuvant therapy in treating breast cancer bone metastasis.

RESULTS

Deprivation of osteoclast-derived ABs reduces the tumor growth and further dissemination of bone metastatic breast cancer

To understand how osteoclast-derived ABs may affect cancer cells in the BME, we used genetically modified apoptosis-deficient MRL/lpr mice[17] to establish animal models of breast cancer bone metastasis by intratibial injection of luciferase-labeled mouse breast cancer 4T-1 cells, followed by weekly observation using bioluminescence imaging (BLI) (Figure 1A). To exclude the effects of luciferase transfection on metastasis formation, we inoculated 4T-1 cells with or without luciferases and observed similar numbers of metastasis foci in other organs from the bone (Figure S1A). The BLI results showed

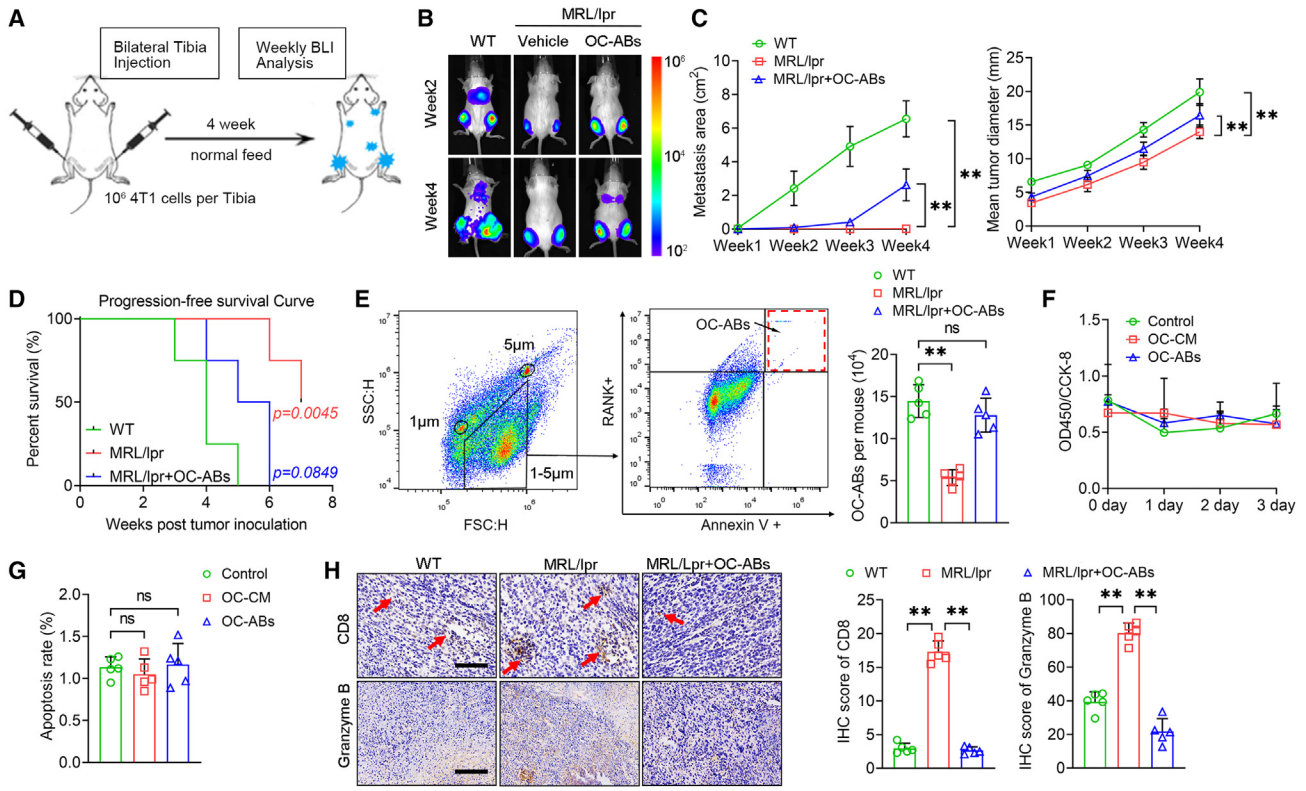

Figure 1. Deprivation of osteoclast-derived ABs reduces the tumor growth and further dissemination of bone metastatic breast cancer

(A) Experimental design of establishing breast cancer bone metastases in mice.

(B) Representative BLI images of tumor growth and secondary metastasis at weeks 2 and 4.

(C) Quantification of secondary metastatic area (cm^2) and mean tumor diameter (mm) in each group of mice, automatically analyzed by software, n = 5.

(D) Kaplan-Meier progression-free survival analysis of mice, n = 4.

(E) Experimental design for counting the total osteoclast (OC)-ABs number from whole bone marrow of mice hind legs by flow cytometry. 1- and 5-μm-diameter beads were used to gate 1- to 5-μm-sized microvesicles. Annexin V^+ and $RANK^+$ events were counted as OC-ABs, n = 5.

(F) Quantification of the proliferative activity of 4T-1 tumor cells cultured with OC-derived conditioned medium (OC-CM; 250 μL/mL) or OC-ABs (15 μg/mL), n = 3.

(G) Quantifying apoptosis rate of 4T-1 tumor cells cultured with OC-CM (250 μL/mL) or OC-ABs (15 μg/mL), n = 5.

(H) Representative IHC for CD8 and granzyme B in bone metastases sections from three groups of mice.

Scale bar of CD8: 100 μm; scale bar of granzyme B: 200 μm; semi-quantitative analysis of CD8 and granzyme B IHC image, n = 5. Red arrows indicate $CD8^+$ cells. The data in each panel represent the means ± SD. P values were obtained by Mantel-Cox test (D) or Student's two-tailed unpaired t test (A–C and E–H), *p < 0.05, **p < 0.01, ns, non-significant.

that the tumor proliferation and further dissemination to distal organs was significantly reduced in MRL/lpr mice relative to the wild-type (WT) mice, marked by smaller tumor size and less metastasis area (Figures 1B and 1C). Interestingly, systemic infusion of osteoclast-ABs, but not ABs derived from other bone-residing cells, resulted in significant tumor growth and further dissemination in MRL/lpr mice (Figures 1B, 1C, and S1B). For survival analysis, the data showed that tumor-bearing WT mice survived for about 5 weeks, and more than half of tumor-bearing MRL/lpr mice survived until the end of 8th week with no relapse; however, systemic restoration of osteoclast-ABs reduced the survival rate of tumor-bearing MRL/lpr mice (Figure 1D).

Using flow cytometry (FCM), we validated that bone tissue and bone marrow (BM) of tumor-bearing MRL/lpr mice contain significantly reduced AB numbers relative to WT mice, which was effectively restored by AB infusion (Figure 1E). To understand the underlying mechanism, we cultured 4T-1 cells using osteoclast conditioned medium (CM) or osteoclast-ABs. The results showed that both osteoclast-CM and osteoclast-ABs had no obvious effect on the proliferation and apoptosis of 4T-1 cells (Figures 1F and 1G), suggesting that osteoclast-ABs might indirectly affect tumor progression. We then sectioned the tumor-bearing bone tissue and used immunohistochemistry (IHC) to evaluate the activity of $CD8^+$ T cells. The results showed that the infiltration and function of $CD8^+$ T cells in the tumor tissues of MRL/lpr mice were stronger than those in the WT and osteoclast-AB restored groups marked by higher $CD8^+$ cell numbers and higher granzyme B activity (Figure 1H), revealing that osteoclast-ABs have an inhibitory effect on $CD8^+$ T cells. Together, our data indicated that breast cancer is less susceptible to growth and further dissemination in the BME lacking osteoclast-ABs and that $CD8^+$ T cell activity is stronger.

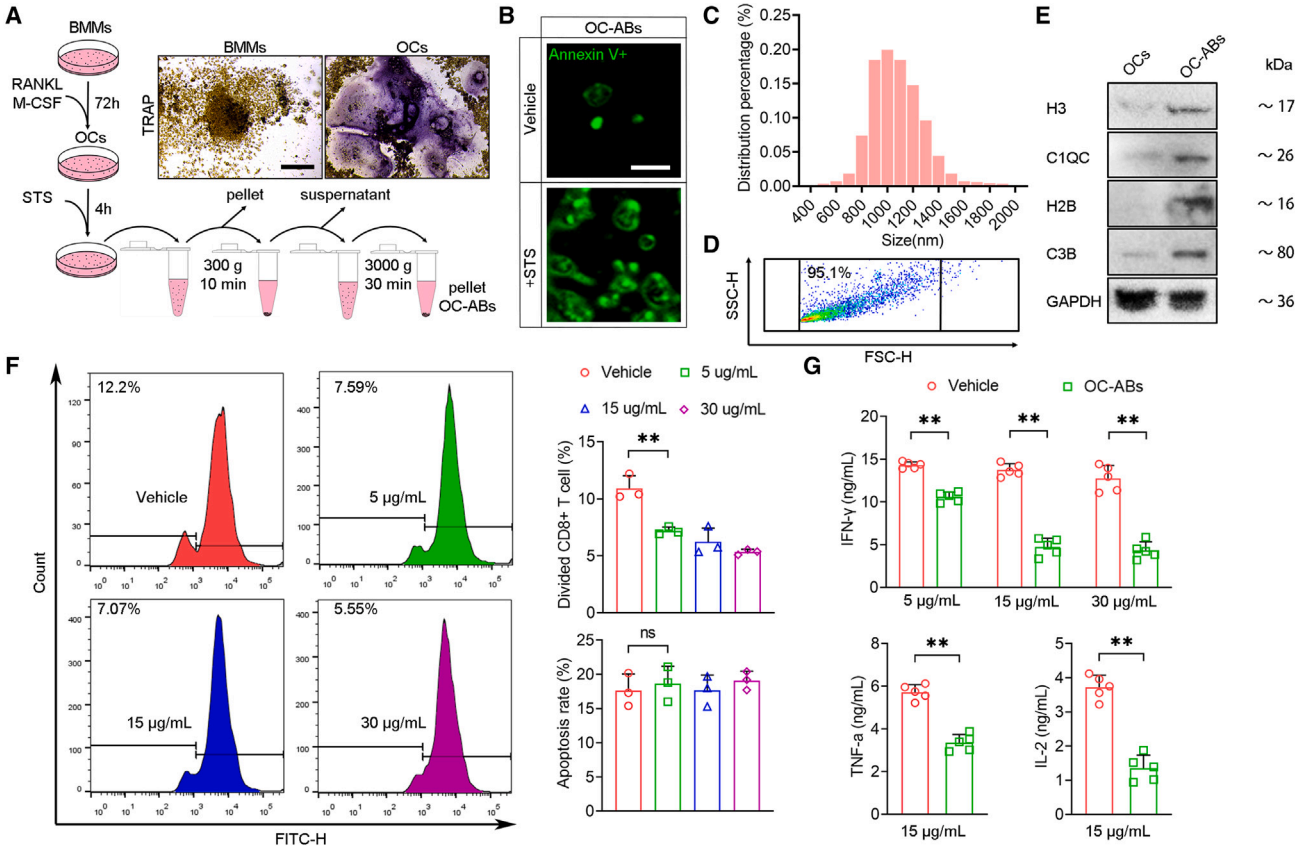

Figure 2. OC-derived Abs inhibit CD8⁺ T cell proliferation and function *in vitro*

(A) Flow chart of osteoclastogenesis induction and OC-ABs extraction. Representative TRAP staining images of bone marrow macrophages (BMMs) and Ocs. Scale bar: 100 μm.

(B) Representative confocal images of OC-ABs (stained with FITC-Annexin V). Scale bar: 2 μm.

(C) Nanoparticle tracking analysis of OC-ABs, n = 3.

(D) Flow cytometry analysis result of OC-ABs purity. 1- and 5-μm-diameter beads were used to gate 1- to 5-μm-sized microvesicles.

(E) Western blot result of H3, C1QC, H2B, and C3B in OC lysate and pelleted OC-ABs.

(F) Representative flow cytometry results of CD8⁺ T cell (stained with CFSE) exposed to OC-ABs for 72 h. Quantification of CD8⁺ T cell division and apoptosis rates, n = 3.

(G) Quantification of IFN-γ, TNF-α, and IL-2 (per well of 24-well plate) secreted by CD8⁺ T cell exposed to OC-ABs for 72 h, n = 5.

The data in each panel represent the means ± SD. p values were obtained by Student's two-tailed unpaired t test, *p < 0.05, **p < 0.01, ns, non-significant.

Osteoclast-derived ABs inhibit CD8⁺ T cell proliferation and function *in vitro*

To study whether osteoclast-ABs directly inhibit CD8⁺ T cell activities, BM macrophages (BMMs) were stimulated to form mature osteoclasts followed by staurosporine (STS) induction for apoptosis and subsequent isolation of ABs by density gradient centrifugation (Figure 2A). Confocal microscopy observation confirmed that the size of osteoclast-ABs is in the range of 1–5 μm (Figure 2B). Nanoparticle tracking analysis revealed that most osteoclast-ABs ranged from 900 to 1,200 nm in diameter (Figure 2C). For FCM analysis, we added 1- and 5-μm fluorescent microspheres as size scales gating osteoclast-ABs. The results confirmed that highly enriched osteoclast-ABs were collected with a purity of about 96% (Figure 2D). For characterization, western blot (WB) analysis revealed a significant enrichment of specific AB markers including histone 3 (H3), C1QC, H2B, and C3B (Figure 2E). We next obtained purified naive CD8⁺ T cells using a sorting kit and cultured them in CM supplemented with osteoclast-ABs (5, 15, and 30 μg/mL). Notably, CD8⁺ T cell proliferation stimulated by 1 μg/mL anti-CD3e was significantly inhibited by the introduction of osteoclast-ABs (Figure 2F), whereas osteoclast-ABs showed no obvious effects on the apoptosis of CD8⁺ T cells (Figure 2F). We further showed that osteoclast-ABs were inhibitory on CD8⁺ T cell activity marked by the decreased secretions of interferon γ (IFN-γ), tumor necrosis factor α (TNF-α), and interleukin-2 (IL-2) detected by enzyme-linked immunosorbent assay (ELISA) (Figure 2G). Concurrently, we examined the effects of BM mesenchymal stem cell (MSC)-derived and chondrocyte-derived ABs on CD8⁺ T cell proliferation, apoptosis, and function *in vitro*, but no significant change was found (Figure S1C). These data implied that osteoclast-ABs play an immunosuppressive effect by inhibiting CD8⁺ T cell proliferation and function.

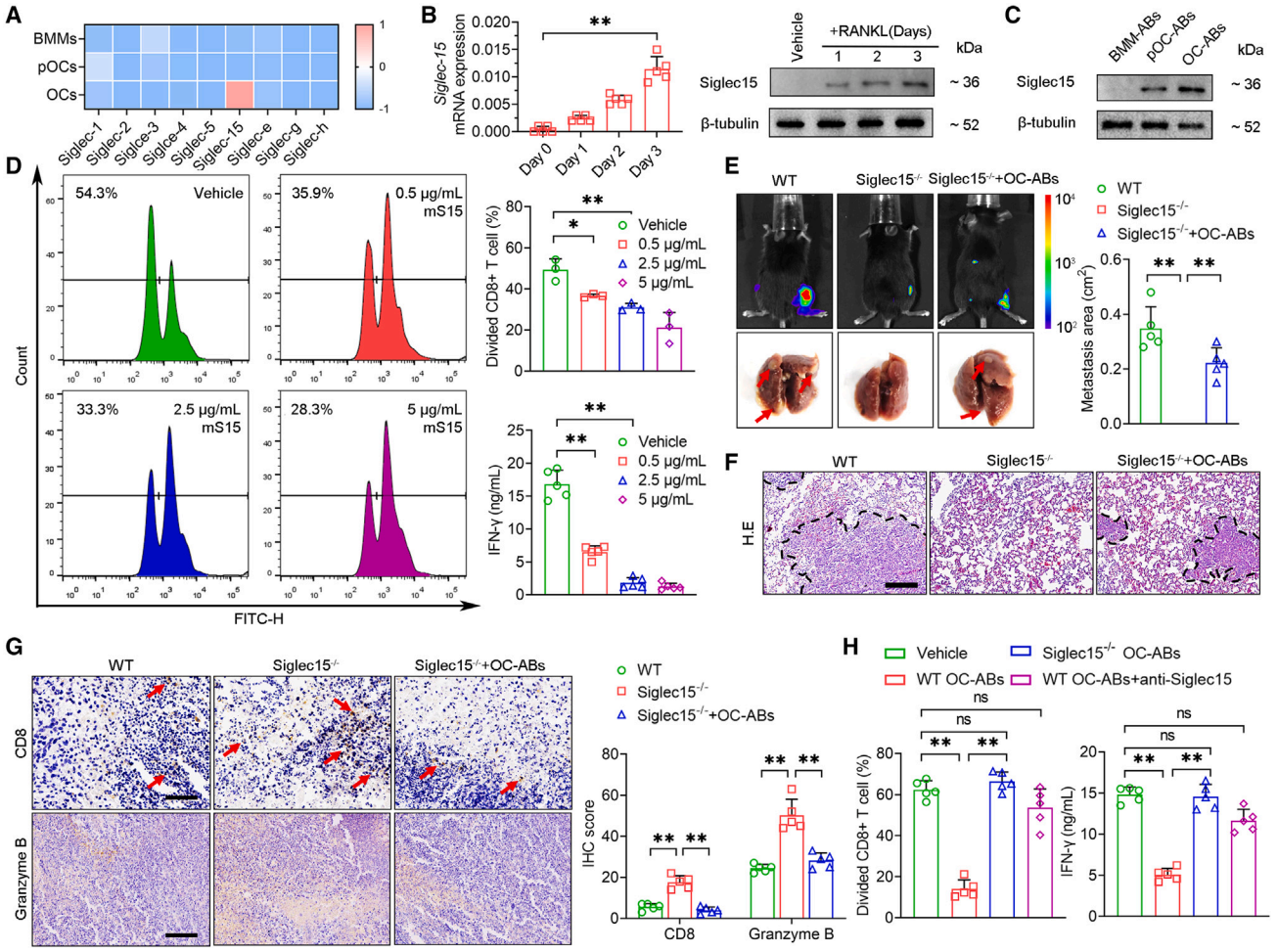

Figure 3. Siglec15 is responsible for the immunosuppressive functions of OC-derived ABs

(A) Heatmap visualized the mRNA expression of *siglec* family genes during OC differentiation and maturation.

(B) Real-time PCR and western blot results showed the mRNA and protein expression of *Siglec15* constantly up-regulated in OCs during differentiation, n = 5.

(C) Western blot showed the Siglec15 expression of apoptotic bodies produced by OCs from different differentiation stages.

(D) Representative flow cytometry results of $CD8^+$ T cells (stained with CFSE) exposed to recombinant mouse Sigcle15 protein for 72 h. Quantification of $CD8^+$ T cell division, n = 3, and IFN-γ secretion level (per well of 24-well plate), n = 5.

(E) Representative BLI images of tumor growth and secondary metastasis in wild-type (WT) mice, Siglec15 knockout mice (*Siglec15*$^{-/-}$), and OC-AB-reinfused *Siglec15*$^{-/-}$ mice (*Siglec15*$^{-/-}$+OC-ABs) at week 2. Quantification of mean metastatic area in three groups of mice (cm^2), n = 5.

(F) Representative H&E staining images of lung tissue from three groups of mice mentioned in section (E), and the black dotted area represents tumor tissue. Scale bar: 100 μm.

(G) Representative IHC image showed the infiltration of $CD8^+$ and granzyme B^+ cells in tumor tissue from three groups of mice mentioned in (E). Scale bar: 100 μm for CD8; scale bar: 200 μm for granzyme B. Red arrows indicate $CD8^+$ cells. Semi-quantitative analysis of CD8 and granzyme B IHC image, n = 5.

(H) The division rate and IFN-γ secretion (per well of 24-well plate) of $CD8^+$ T cells (stained with CFSE), which were separately exposed to 15 μg/mL WT mouse-derived OC-ABs (WT-OC-ABs), *Siglec15*$^{-/-}$ mouse-derived OC-ABs (*Siglec15*$^{-/-}$-OC-ABs), and recombinant Siglec15 antibody pre-incubated WT OCs-ABs (WT-OC-ABs+anti-Siglec15) or not, n = 5.

The data in each panel represent the means ± SD. p values were obtained by Student's two-tailed unpaired t test, *p < 0.05, **p < 0.01, ns, non-significant.

Siglec15 is responsible for the immunosuppressive functions of osteoclast-derived ABs

The transcriptomic profile of Siglec family was clustered using RNA sequencing (RNA-seq) (GEO: GSE133515), suggesting that Siglec15 is the only up-regulated Siglec during osteoclast differentiation (Figure 3A). The upregulation of Siglec15 transcription and translation was validated by qPCR and WB (Figure 3B). We then isolated ABs derived from BMMs, preosteoclasts, and osteoclasts for WB analysis, and the results showed that Siglec15 was expressed in ABs derived from preosteoclasts and mature osteoclasts but not from BMMs (Figure 3C). Moreover, with quantitative total protein, we compared the expression of Siglec15 among ABs, small extracellular vesicles (sEVs), and parental osteoclasts and found that Siglec15 expression was mostly enriched in ABs (Figure S1D). We then introduced recombinant mouse Siglec15 (mS15) with different

dosages (0.5, 2.5, or 5 μg/mL) into anti-CD3e-mediated $CD8^+$ T cell activation, followed by carboxyfluorescein succinimidyl ester (CFSE) staining, FCM, and ELISA analyses. The results showed that mS15 inhibits $CD8^+$ T cell proliferation and function in a dose-dependent manner marked by decreased dividing rate and IFN-γ secretion (Figure 3D).

To further elucidate the immunosuppressive effects of Siglec15 from osteoclast-ABs, we established breast cancer bone metastasis model using *Siglec15*$^{-/-}$ mice. Mice deficient of Siglec15 exhibited a strong anti-tumor capacity marked by low *in situ* tumor growth and not a single case of further dissemination to lungs. Nevertheless, restoration of osteoclast-ABs by systemic reinfusion blunted the anti-tumor properties of *Siglec15*$^{-/-}$ mice, marked by progressive tumor proliferation and occasional secondary metastases (Figures 3E and 3F). IHC staining results showed that tumor tissues from *Siglec15*$^{-/-}$ mice had the highest number of $CD8^+$ cells and the highest amount of granzyme B activity, indicating the highest infiltration degree of $CD8^+$ T cells (Figure 3G). To further confirm the immunosuppressive effects of Siglec15 from osteoclast-ABs, we extracted osteoclasts from *Siglec15*$^{fl/fl}$ (WT) mice and *Siglec15*$^{-/-}$ mice for ABs generations. Subsequently, we added WT mouse-derived osteoclast-ABs (WT-OC-ABs), *Siglec15*$^{-/-}$ mouse-derived OC-ABs (*Siglec15*$^{-/-}$-OC-ABs), and recombinant Siglec15 antibody pre-incubated WT-OCs-ABs to the naive $CD8^+$ T cell culture system. The results revealed that *Siglec15*$^{-/-}$-OC-ABs had no inhibitory effect on the activation or the IFN-γ secretion of $CD8^+$ T cells; likewise, the recombinant antibody blocked Siglec15 and relived the immunosuppressive effects of WT-OC-ABs (Figure 3H). The inhibitory effects of Siglec15 on OC-ABs were also validated using human OC and $CD8^+$ T cells (Figures S2A and S2B). These data suggested that Siglec15 is the key molecule responsible for the immunosuppressive functions of OC-ABs.

Siglec15 binds with α-2,6 sialic acid-modified TLR2, suppressing the activation of naive $CD8^+$ T cells

To explore the underlying immunosuppressive mechanism of Siglec15, we detected the effects of Siglec15 on naive and activated $CD8^+$ T cells, respectively. Specifically, mS15 was introduced into anti-CD3e-stimulated naive $CD8^+$ T cells on days 1 or 3 and then was expanded for 72 h before further tests (Figure 4A). FCM analysis and ELISA results showed that the proliferation and immune-related factor (IFN-γ, TNF-α, IL-2) secretion of naive $CD8^+$ T cells were significantly inhibited by mS15, while activated $CD8^+$ T cells were not affected (Figures 4B and 4C). To determine the binding targets of Siglec15, we used a liquid chromatography-mass spectrometry (LC-MS) dataset (ProteomeXchange Consortium, PXD006359) identifying Siglec15-interacting proteins using proximity-labeling methods.[18] The *cis* proximity-labeling data have their limitations but did suggest that, among the 318 potential Siglec15-binding targets, Toll-like receptor 2 (TLR2) was screened out with a combination of high scoring and better biological relevance (Figure 4D). It has been reported that TLR2 is abundantly expressed on $CD8^+$ T cells as a co-stimulatory receptor.[19,20]

For validation, we extracted the total protein of $CD8^+$ T cells exposed to OC-ABs for co-immunoprecipitation (coIP) assays. The coIP results confirmed the reciprocal bindings of Siglec15 and TLR2; however, the bindings can be disrupted by the introduction of sialidase, suggesting that sialic acids mediated the TLR2-Siglec15 interaction (Figure 4E). Because Siglec15 characteristically exerts biological functions by binding to sialic acid (SA) residues α-2,3, or α-2,6 on the surface of glycosylated receptors in mammals,[21] we asked how Siglec15 binds to TLR2 in $CD8^+$ T cell activation. Therefore, we immunoprecipitated TLR2 from $CD8^+$ T cells and used fluorescein isothiocyanate (FITC)-labeled biotin Maackia amurensis lectin-II (MAL-II) or Sambucus nigra agglutinin (SNA) to bind SA residue α-2,3 or α-2,6 of glycosylated TLR2. The results of liquid-phase fluorescence intensity detection implied that TLR2 of $CD8^+$ T cells is mainly modified by α-2,6 SA residues (Figures 4F and S2C). However, the affinity of SNA for α-2,6 SA does not allow us to conclusively determine that the binding partner of S15 is exclusively α-2,6 SA.

Siglec15 inhibits naive $CD8^+$ T cell activation via blocking TLR2 co-stimulatory signaling pathways

To study how Siglec15-TLR2 interaction inhibits naive $CD8^+$ T cell activation, we cultured naive $CD8^+$ T cells using TLR2 agonist Pam3CSK4, Siglec15, and sialidase. FCM analysis showed that Pam3CSK4 promoted $CD8^+$ T cell activities, as evidenced by increased proliferation and cytokine secretion, whereas the addition of Siglec15 robustly weakened this enhancement. Notably, the suppressive effects of Siglec15 can be significantly alleviated by the introduction of sialidase, disrupting Siglec15-TLR2 interactions (Figures 5A and 5B). We then studied the effects of Siglec15 binding on TLR2 downstream co-stimulatory signaling. The WB result showed that the expression of IRAK4, TRAF6, and TAK1 was upregulated in response to Pam3CSK4, while co-exposure of Siglec15 reversed the activation. As expected, sialidase treatment uncoupling Siglec15-TLR2 interactions restored the activation potency of Pam3CSK4 on TLR2 co-stimulatory signaling (Figures 5C and S3B). Moreover, IHC staining and quantitative analysis showed that the number of $IRAK4^+$, $TRAF6^+$, and $TAK1^+$ cells in the bone metastases tumor tissue from MRL/lpr mice was higher than that of WT mice, and MRL/lpr mice systemically reinfused with OC-ABs (Figures 5D and 5E). Together, our data suggested that Siglec15 on OC-ABs could suppress naive $CD8^+$ T cell activation via binding with TLR2 and by blocking the downstream co-stimulatory signaling.

Siglec15 neutralizing antibodies reduced secondary metastasis and improved survival rate in mice with advanced breast cancer bone metastases

We generated a Siglec-15-specific neutralizing monoclonal antibody (mAb; S15 NAB) using recombinant antibody technology to target the immunoregulatory function of Siglec-15. We validated its binding to both human and mouse Siglec-15 using ELISA (Figure S3A). Mice with advanced breast cancer bone metastasis were treated with sialidase (NAU), alendronate sodium (ALN), or S15 NAB for observing of tumor proliferation, secondary metastasis, and progression-free survival (Figure 6A). At week 2, BLI results revealed a rapid tumor growth and secondary metastasis in the PBS- and ALN-treated mice but not the NAU- and S15 NAB-treated mice. At week 4, a large number of secondary metastases

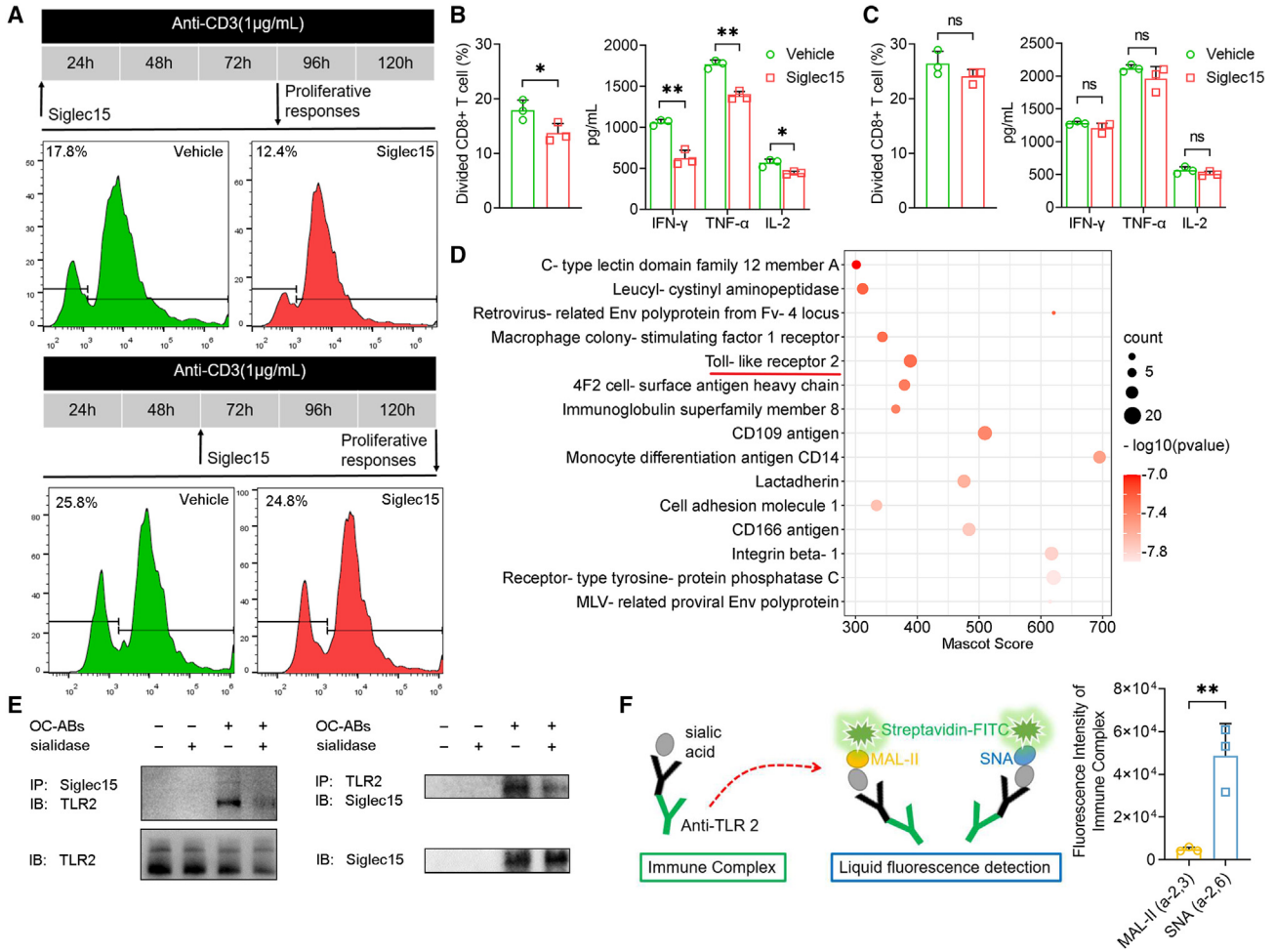

Figure 4. Siglec15 binds with α-2,6 sialic acid-modified TLR2, suppressing the activation of naive CD8⁺ T cells

(A) Experimental design for exploring the stage of CD8⁺ T cells affected by Siglec15 and the representative flow cytometry results of CD8⁺ T cell (stained with CFSE) exposed to Siglec15 for 72 h.

(B) The division rate of CD8⁺ T cells exposed early to Siglec15 for 72 h and the quantification of IFN-γ, TNF-α, and IL-2 (per well of 96-well plate) secretion, n = 3.

(C) The division rate of CD8⁺ T cells exposed late to Siglec15 for 72 h and the quantification of IFN-γ, TNF-α, and IL-2 (per well of 96-well plate) secretion, n = 3.

(D) Bubble plot showing the collection of glyco-membrane proteins bound to Siglec15. Criteria: $7 < -\log10(p) < 1.3$, 3 < unique peptide, 300 < Mascot score < 700.

(E) Immunoblotting (IB) for TLR2 in whole CD8⁺ T cell lysates or protein complexes immunoprecipitated (IP) with Siglec15 (top); IB for Siglec15 in whole CD8⁺ T cell lysates or protein complexes IP with TLR2 (bottom). CD8⁺ T cells were exposed to OC-ABs for 24 h with or without sialidase (0.2 U/mL) before co-immunoprecipitation.

(F) Experimental design for detecting TLR2-bound sialic acid residue type by co-immunoprecipitation, and liquid-phase fluorescence intensity quantification of biotin-bound TLR2, n = 3.

The data in each panel represent the means ± SD and were analyzed by Student's two-tailed unpaired t test, *p < 0.05, **p < 0.01, ns, non-significant.

occurred in the PBS- and ALN-treated mice with no significant difference in between; however, only a small number of secondary metastases were detected in the NAU-treated mice, and no secondary metastases were detected in mice treated with S15 NAB (Figures 6B and 6C). ALN-treated mice exhibited increased OC-AB amounts (Figure S3C). We measured and recorded the tumor size of bone metastases, finding that although NAU, ALN, and S15 NAB all slowed down tumor proliferation in the first 2 weeks, only S15 NAB continued the anti-tumor activity until the end of week 4 (Figure 6D). Progression-free survival analysis showed that S15 NAB significantly increased the survival of mice with advanced breast cancer bone metastases marked by the lowest mortality rate (p = 0.0018), whereas the survival of the NAU- or ALN-treated mice were not statistically different relative to the control group (Figure 6E). For evaluation of secondary metastasis from bone, we dissected the lungs to identify the number of metastasis sites. Quantification analysis verified that NAU and S15 NAB could effectively reduce the occurrence of secondary metastases from bone (Figure 6F). IHC staining and consequent statistical analysis of breast cancer bone metastases tissue showed that NAU and S15 NAB treatments could significantly increase the number of CD8⁺ and granzyme B⁺ cells in tumor tissue, implicating a higher CD8⁺ T cell infiltration and activity (Figure 6G). For validation, we conducted multiplexed immunofluorescence staining to examine

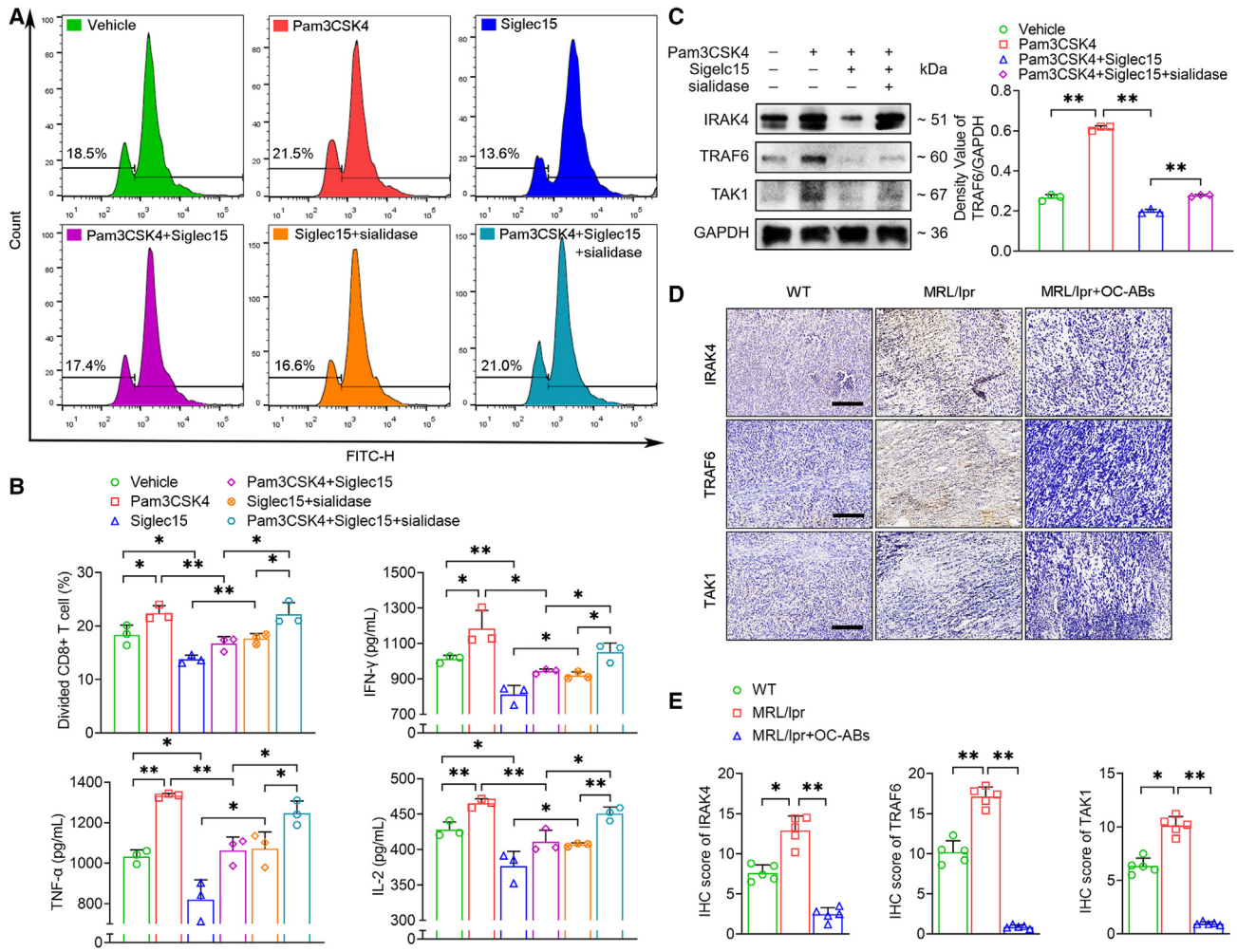

Figure 5. Siglec15 inhibits naive CD8$^+$ T cell activation via blocking TLR2 co-stimulatory signaling pathways

(A) Representative flow cytometry results of CD8$^+$ T cell (stained with CFSE) exposed to different treatments.

(B) Quantification of CD8$^+$ T cell division and immune secretion (IFN-γ, TNF-α, IL-2; per well of 96-well plate), n = 3.

(C) Western blot result showed expression of IRAK4, TRAF6, and TAK1 in CD8$^+$ T cell lysate after different treatments, and quantification of the relative expression of TRAF6 in CD8$^+$ T cells under different treatments, n = 3.

(D) Representative IHC for IRAK4, TRAF6, and TAK1 in bone metastases sections from three groups of mice. Scale bar: 200 μm.

(E) Semi-quantitative analysis of IRAK4, TRAF6, and TAK1 IHC staining images, n = 5.

The data in each panel represent the means ± SD and were analyzed by Student's two-tailed unpaired t test, *p < 0.05, **p < 0.01.

the correlation between Siglec-15 expression and T cell activity. The results demonstrate that mice treated with anti-S15 exhibit significantly increased CD8$^+$ T cell infiltrations and granzyme B expression (Figure S3D). This suggests that anti-S15 treatment may enhance the immune response mediated by CD8$^+$ T cells. To evaluate the bone-protective effects of S15 NAB, we compared its effects with those of alendronate treatment, as well as with those of NAU and PBS controls. The microcomputed tomography (micro-CT) results showed that S15 NAB and alendronate treatments maintained bone volume to a similar extent, with both significantly higher than NAU and PBS controls (Figure S4). To further validate the therapeutic potential of S15 NAB in secondary metastasis, we repeated some of the key experiments using the MA-891 and EMT-6 cell lines of mouse breast cancer. While MA-891 failed to disseminate to other organs from bone, EMT-6 cells showed a similar pattern with 4T-1, demonstrating the ability to form metastasis foci in other organs. In mice with advanced breast cancer bone metastases, treatment with S15 NAB significantly increased survival (Figure S5). The data presented above demonstrate the effectiveness of neutralizing Siglec15 with mAbs in both bone protection and elimination of its immunosuppressive function. These results suggest that this approach may have therapeutic potential for the treatment of advanced breast cancer bone metastases.

DISCUSSION

Our study shows that OC-derived ABs suppress the activation of naive CD8$^+$ T cells, thereby promoting the dissemination of

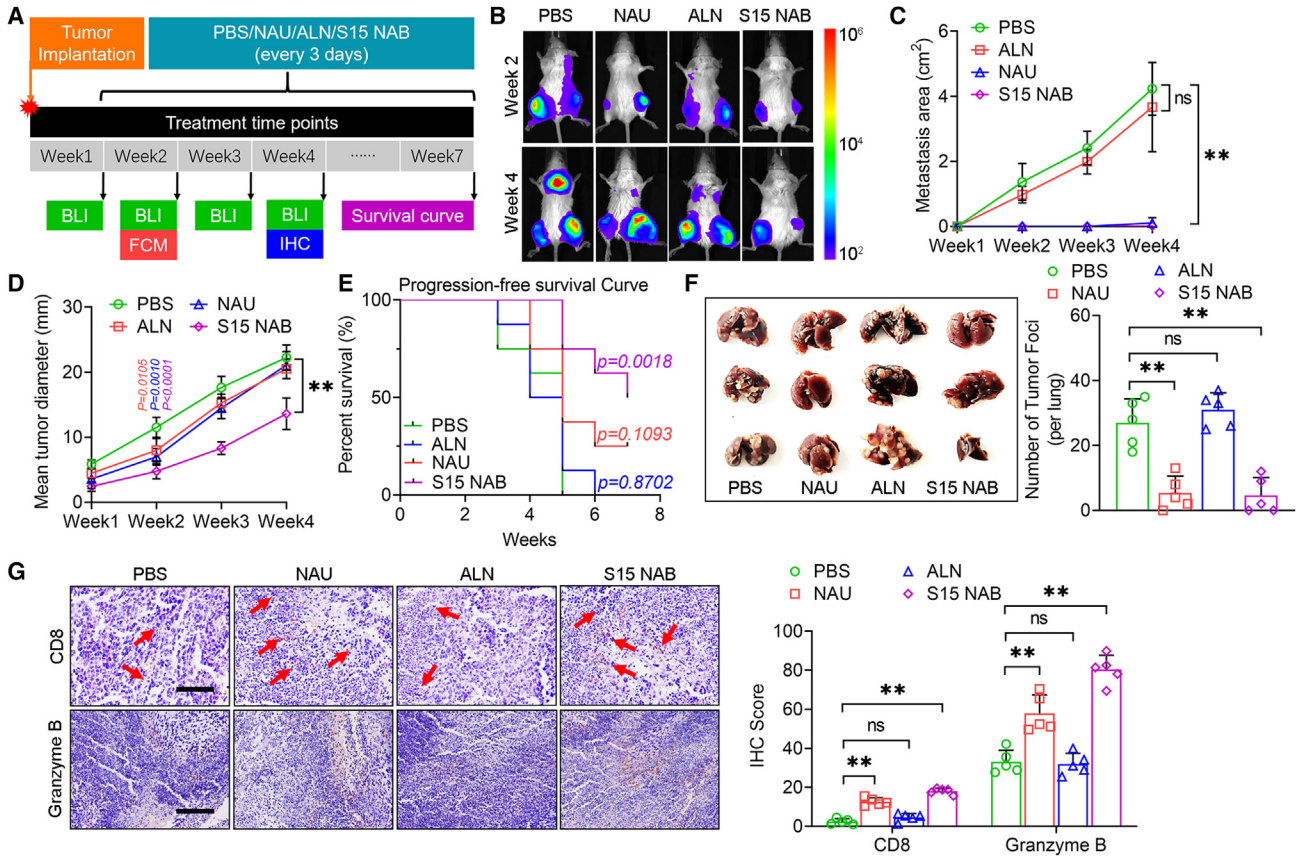

Figure 6. Siglec15 neutralizing antibodies reduced secondary metastasis and improved survival rate in mice with advanced breast cancer bone metastases

(A) Experimental design for exploring the progress of breast cancer bone metastasis under the action of different therapeutic drugs (Siglec15 neutralizing antibody, intraperitoneal [i.p.], S15 NAB; neuraminidase, 0.2 U/per tibia, intramuscular [i.m.], NAU; alendronate sodium, 2 mg/kg, i.p., ALN).

(B) Representative BLI images of tumor growth and secondary metastasis at the weeks 2 and 4.

(C) Quantification of secondary metastatic area (cm^2) in each group of mice, automatically analyzed by software, n = 5.

(D) Quantification of mean tumor diameter (mm) in each group of mice, automatically analyzed by software, n = 5.

(E) Kaplan-Meier progression-free survival analysis of four groups of mice treated with PBS, ALN, NAU, and S-15 NAB, n = 8.

(F) Representative gross pictures of lung anatomy from the four groups of mice at week 4 and the counting results of tumor foci on lung, n = 5.

(G) Representative IHC image in bone metastases sections from four groups of mice.

Scale bar: 100 μm for CD8; scale bar: 200 μm for granzyme B; semi-quantitative analysis of CD8 and granzyme B IHC image, n = 5. Red arrows indicate $CD8^+$ cells. The data in each panel represent the means ± SD. p values were obtained by Mantel-Cox test (E) or Student's two-tailed unpaired t test (A–D, F, and G), *p < 0.05, **p < 0.01, ns, non-significant.

breast cancer cells from the BME. Specifically, we found that Siglec15 on OC-derived ABs binds to TLR2 molecules modified by α-2,6 SA on naive $CD8^+$ T cells, leading to the suppression of co-stimulatory signaling and to an increase in the activation threshold. These findings provide insights into the mechanisms underlying breast cancer bone metastasis and further dissemination and suggest potential therapeutic targets for preventing this process (Figure S6). Our data potentially explained why targeting OCs using BPs cannot extend the overall survival of patients with breast cancer bone metastases.[11] BPs can effectively eliminate the bone-resorbing OCs via inducing cell apoptosis[22]; however, the ABs produced by OC apoptosis could not be reduced but rather increased due to the action of BPs. The animal study results showed that in comparison with ALN, neutralizing mAbs against Siglec15 reached better outcomes in inhibiting tumor growth, enhancing local $CD8^+$ T cell function, reducing tumor secondary metastasis, and increasing survival rate in mice with advanced breast cancer bone metastasis.

In osteolytic breast cancer metastasis, the vicious cycle in the bone remodeling compartment is a well-accepted paradigm describing the interactions of cancer cells and bone-residing cells.[23,24] OC plays a central role in this paradigm by degrading bone tissue and releasing growth factors within the bone matrix.[23,25,26] In clinical practice, anti-bone resorption has been recognized as an adjuvant therapy treating breast cancer metastasis, though the prevention of cancer relapse and the increase of survival time are limited.[4,27,28] We also noticed the limitations of BP treatment in improving the survival of mice with advanced breast cancer bone

metastasis. Pharmacologically, BPs induce cell apoptosis of OCs,[29,30] increasing the amounts of immunosuppressive OC-ABs in the bone-tumor niche, thus hindering the function of $CD8^+$ T cells.

Siglec15 suppresses T cell activation, and antibody against Siglec15 shows huge potential in cancer immunotherapy.[31] In the TME, Siglec15-expressing cancer cells and tumor-associated macrophages facilitate tumor growth and metastasis via suppressing T cell activation.[32] We showed that Siglec15 is most enriched in OC-ABs relative to OCs and other EVs, making OC-ABs one of the major sources of Siglec15 in the bone-tumor niche of breast cancer. Siglec15 is now considered an immune checkpoint molecule that can inhibit T cell activities,[33,34] but the signaling mechanisms are not known, as the receptor for Siglec15 has not been identified. Here, we uncovered that sialylated TLR2 binds to Siglec15 as its receptor. TLR2 is expressed in both T cells and macrophages with regulatory roles for their effector functions and activation.[20,35] We showed that naive $CD8^+$ T cells have significantly higher cell surface sialylation levels relative to activated T cells, facilitating the binding of Siglec15. Drugs that regulate TLR2-related costimulatory signals are increasingly used as adjuvants for the treatment of cancer vaccines and tumor immunotherapeutics.[36–38] Interestingly, we previously reported that Siglec15 is essential for RANKL-induced osteoclastogenesis and that blockade of Siglec15 abrogates OC formation.[16] This makes Siglec15 a common target for both anti-bone resorption and immunotherapy.

More and more studies are confirming the critical role of aberrant sialylation and SA metabolism in cancer progression and metastasis.[39–41] In breast cancer metastasis, hypersialylation is correlated with the formation of remote metastasis.[42] It has been reported that both salivary and serum SA concentrations were elevated in patients with breast cancer.[43,44] The change of glycosylation has been shown to be useful for diagnosis, determination of tumor stage, and prognosis.[45] Our study showed the molecular involvement of α-2,6 sialylation in mediating Siglec15-TLR2 binding in $CD8^+$ T cell suppression, which is a potential target for therapeutic strategies. Moreover, the cause of increased α-2,6 sialylation might be due to the change in gene expression of relative glycosyltransferases,[46] which is worth being explored further. In this study, we also demonstrated that sialidase treatments limited the progression and metastasis of breast cancer, though similar effects were found in suppressing human bladder cancer.[47] Nevertheless, unlike the S15 NAB, sialidase treatments failed to increase the survival of mice with advanced bone breast cancer metastasis. The difference might be due to the non-specificity of sialidase causing the depletion of other subtype functional SAs. Though less studied, apoptotic cell-derived vesicles have been shown to be functional in cancer immunity and metastasis.[48,49] In glioblastoma, tumor-derived ABs were shown to promote cancer cell proliferation and therapy resistance.[50] Unlike tumor-derived ABs, OC-derived ABs are residing components of the tumor-bone niche due to the constant bone remodeling.

Our data highlighted the improved survival of mice with advanced breast cancer bone metastasis treated with S15 NAB relative to those treated with BPs. Our study also supports Siglec15 as an attractive cell surface target for immunotherapy in patients with breast cancer bone metastasis, as the blockade of Siglec15 simultaneously inhibits OC formation and frees naive $CD8^+$ T cells to further activation.

Limitations of the study

To prove that Siglec-15 is a general strategy for cancer treatment, we have incorporated two additional models, MA-891 and EMT-6. The data showed that MA-891 cells could not create secondary metastasis from bone to distal organs. Therefore, mice were all alive 8 weeks after the modeling. Currently, there is limited research and international recognition surrounding MA-891 as a breast cancer model. Although it is reported to be a highly metastatic tumor, there is insufficient evidence supporting its specific bone metastatic characteristics and secondary metastasis. The data from *cis* proximity-labeling LC-MS are only suggestive and need to be further validated by low-throughput assays like coIP. While we acknowledge that TLR2 may not be the most specific function of Siglec15, our current data led us to conclude that Siglec15 influences the downstream signaling of TLR2 in CD8 T cells. We acknowledge that the affinity of SNA does not allow us to conclusively determine that the binding partner of Siglec15 is exclusively α-2,6 SA.

STAR★METHODS

Detailed methods are provided in the online version of this paper and include the following:

- KEY RESOURCES TABLE
- RESOURCE AVAILABILITY
  - Lead contact
  - Materials availability
  - Data and code availability
- EXPERIMENTAL MODEL AND SUBJECT DETAILS
  - *In vivo* animal studies
  - Cell lines and primary cultures
- METHOD DETAILS
  - Cell counting Kit-8 test
  - Induction of osteoclastogenesis and apoptosis
  - Apoptotic body extraction and identification
  - Establishment of breast cancer bone metastases mouse model and treatment
  - Bioluminescence imaging
  - Generation of Siglec15 neutralizing antibodies
  - Immunohistochemistry and immunofluorescence staining
  - $CD8^+$ T cell sorting and proliferation assay
  - Enzyme-linked immunosorbent (ELISA) assay
  - Multiple fluorescence staining
  - Micro-CT
  - Real-time PCR (PCR)
  - Western blot analysis and co-immunoprecipitation analysis
  - RNA-seq
- QUANTIFICATION AND STATISTICAL ANALYSIS

SUPPLEMENTAL INFORMATION

Supplemental information can be found online at https://doi.org/10.1016/j.xcrm.2023.101165.

ACKNOWLEDGMENTS

This work was funded by a grant from the National Natural Science Foundation of China (82172489), a grant from the TMMU of clinical innovation funding (CX2019LC121), fundings for young investigators of PLA (2022-JCJQ-QT-004), and fundings for young investigators of Southwest Hospital, TMMU (XZ-2019-505-005).

AUTHOR CONTRIBUTIONS

Conceived and designed the study, Y.W. and C.D.; performed experiments, Y.W., H.A, Y.X., and J.T.; software, data curation, and visualization, Y.W. and H.A.; analyzed the data, Y.W., C.D., and H.A.; provided advice and technical assistance, J.X. and F.L.; writing – original draft, Y.W. and H.A.; writing – review & editing, Y.W., C.D., and H.A.; supervision, J.X. and F.L.; project administration, C.D., J.X., and F.L.; funding acquisition, C.D., J.X., and F.L. All authors read and approved the final manuscript.

DECLARATION OF INTERESTS

The authors declare no competing interests.

INCLUSION AND DIVERSITY

We support inclusive, diverse, and equitable conduct of research.

Received: October 18, 2022
Revised: April 18, 2023
Accepted: July 31, 2023
Published: August 21, 2023

REFERENCES

1. Coleman, R.E., Croucher, P.I., Padhani, A.R., Clezardin, P., Chow, E., Fallon, M., Guise, T., Colangeli, S., Capanna, R., and Costa, L. (2020). Bone metastases. Nat. Rev. Dis. Prim. *6*, 83. https://doi.org/10.1038/s41572-020-00216-3.
2. Zhang, W., Bado, I.L., Hu, J., Wan, Y.W., Wu, L., Wang, H., Gao, Y., Jeong, H.H., Xu, Z., Hao, X., et al. (2021). The bone microenvironment invigorates metastatic seeds for further dissemination. Cell *184*, 2471–2486.e2420. https://doi.org/10.1016/j.cell.2021.03.011.
3. Hofbauer, L.C., Rachner, T.D., Coleman, R.E., and Jakob, F. (2014). Endocrine aspects of bone metastases. Lancet Diabetes Endocrinol. *2*, 500–512. https://doi.org/10.1016/S2213-8587(13)70203-1.
4. Friedl, T.W.P., Fehm, T., Muller, V., Lichtenegger, W., Blohmer, J., Lorenz, R., Forstbauer, H., Fink, V., Bekes, I., Huober, J., et al. (2021). Prognosis of Patients With Early Breast Cancer Receiving 5 Years vs 2 Years of Adjuvant Bisphosphonate Treatment: A Phase 3 Randomized Clinical Trial. JAMA Oncol. *7*, 1149–1157. https://doi.org/10.1001/jamaoncol.2021.1854.
5. Raggatt, L.J., and Partridge, N.C. (2010). Cellular and molecular mechanisms of bone remodeling. J. Biol. Chem. *285*, 25103–25108. https://doi.org/10.1074/jbc.R109.041087.
6. Ma, Q., Liang, M., Wu, Y., Ding, N., Duan, L., Yu, T., Bai, Y., Kang, F., Dong, S., Xu, J., and Dou, C. (2019). Mature osteoclast-derived apoptotic bodies promote osteogenic differentiation via RANKL-mediated reverse signaling. J. Biol. Chem. *294*, 11240–11247. https://doi.org/10.1074/jbc.RA119.007625.
7. Ma, Q., Liang, M., Limjunyawong, N., Dan, Y., Xing, J., Li, J., Xu, J., and Dou, C. (2020). Osteoclast-derived apoptotic bodies show extended biological effects of parental cell in promoting bone defect healing. Theranostics *10*, 6825–6838. https://doi.org/10.7150/thno.45170.
8. Ma, Q., Liang, M., Wu, Y., Luo, F., Ma, Z., Dong, S., Xu, J., and Dou, C. (2021). Osteoclast-derived apoptotic bodies couple bone resorption and formation in bone remodeling. Bone Res *9*, 5. https://doi.org/10.1038/s41413-020-00121-1.
9. Raskov, H., Orhan, A., Christensen, J.P., and Gogenur, I. (2021). Cytotoxic CD8(+) T cells in cancer and cancer immunotherapy. Br. J. Cancer *124*, 359–367. https://doi.org/10.1038/s41416-020-01048-4.
10. Li, K., Li, T., Feng, Z., Huang, M., Wei, L., Yan, Z., Long, M., Hu, Q., Wang, J., Liu, S., et al. (2021). CD8(+) T cell immunity blocks the metastasis of carcinogen-exposed breast cancer. Sci. Adv. *7*. https://doi.org/10.1126/sciadv.abd8936.
11. Ali, H.R., Provenzano, E., Dawson, S.J., Blows, F.M., Liu, B., Shah, M., Earl, H.M., Poole, C.J., Hiller, L., Dunn, J.A., et al. (2014). Association between CD8+ T-cell infiltration and breast cancer survival in 12,439 patients. Ann. Oncol. *25*, 1536–1543. https://doi.org/10.1093/annonc/mdu191.
12. Vihervuori, H., Autere, T.A., Repo, H., Kurki, S., Kallio, L., Lintunen, M.M., Talvinen, K., and Kronqvist, P. (2019). Tumor-infiltrating lymphocytes and CD8(+) T cells predict survival of triple-negative breast cancer. J. Cancer Res. Clin. Oncol. *145*, 3105–3114. https://doi.org/10.1007/s00432-019-03036-5.
13. Ibrahim, E.M., Al-Foheidi, M.E., Al-Mansour, M.M., and Kazkaz, G.A. (2014). The prognostic value of tumor-infiltrating lymphocytes in triple-negative breast cancer: a meta-analysis. Breast Cancer Res. Treat. *148*, 467–476. https://doi.org/10.1007/s10549-014-3185-2.
14. Nanda, R., Chow, L.Q., Dees, E.C., Berger, R., Gupta, S., Geva, R., Pusztai, L., Pathiraja, K., Aktan, G., Cheng, J.D., et al. (2016). Pembrolizumab in Patients With Advanced Triple-Negative Breast Cancer: Phase Ib KEYNOTE-012 Study. J. Clin. Oncol. *34*, 2460–2467. https://doi.org/10.1200/JCO.2015.64.8931.
15. Wang, J., Sun, J., Liu, L.N., Flies, D.B., Nie, X., Toki, M., Zhang, J., Song, C., Zarr, M., Zhou, X., et al. (2019). Siglec-15 as an immune suppressor and potential target for normalization cancer immunotherapy. Nat. Med. *25*, 656–666. https://doi.org/10.1038/s41591-019-0374-x.
16. Dou, C., Zhen, G., Dan, Y., Wan, M., Limjunyawong, N., and Cao, X. (2022). Sialylation of TLR2 initiates osteoclast fusion. Bone Res *10*, 24. https://doi.org/10.1038/s41413-022-00186-0.
17. Watson, M.L., Rao, J.K., Gilkeson, G.S., Ruiz, P., Eicher, E.M., Pisetsky, D.S., Matsuzawa, A., Rochelle, J.M., and Seldin, M.F. (1992). Genetic analysis of MRL-lpr mice: relationship of the Fas apoptosis gene to disease manifestations and renal disease-modifying loci. J. Exp. Med. *176*, 1645–1656. https://doi.org/10.1084/jem.176.6.1645.
18. Chang, L., Chen, Y.J., Fan, C.Y., Tang, C.J., Chen, Y.H., Low, P.Y., Ventura, A., Lin, C.C., Chen, Y.J., and Angata, T. (2017). Identification of Siglec Ligands Using a Proximity Labeling Method. J. Proteome Res. *16*, 3929–3941. https://doi.org/10.1021/acs.jproteome.7b00625.
19. Geng, D., Zheng, L., Srivastava, R., Asprodites, N., Velasco-Gonzalez, C., and Davila, E. (2010). When Toll-like receptor and T-cell receptor signals collide: a mechanism for enhanced CD8 T-cell effector function. Blood *116*, 3494–3504. https://doi.org/10.1182/blood-2010-02-268169.
20. Komai-Koma, M., Jones, L., Ogg, G.S., Xu, D., and Liew, F.Y. (2004). TLR2 is expressed on activated T cells as a costimulatory receptor. Proc. Natl. Acad. Sci. USA *101*, 3029–3034. https://doi.org/10.1073/pnas.0400171101.
21. Smith, B.A.H., and Bertozzi, C.R. (2021). The clinical impact of glycobiology: targeting selectins, Siglecs and mammalian glycans. Nat. Rev. Drug Discov. *20*, 217–243. https://doi.org/10.1038/s41573-020-00093-1.
22. Rogers, M.J., Gordon, S., Benford, H.L., Coxon, F.P., Luckman, S.P., Monkkonen, J., and Frith, J.C. (2000). Cellular and molecular mechanisms of action of bisphosphonates. Cancer *88*, 2961–2978. https://doi.org/10.1002/1097-0142(20000615)88:12+<2961::aid-cncr12>3.3.co;2-c.

23. Chen, Y.C., Sosnoski, D.M., and Mastro, A.M. (2010). Breast cancer metastasis to the bone: mechanisms of bone loss. Breast Cancer Res. *12*, 215. https://doi.org/10.1186/bcr2781.

24. Onishi, T., Hayashi, N., Theriault, R.L., Hortobagyi, G.N., and Ueno, N.T. (2010). Future directions of bone-targeted therapy for metastatic breast cancer. Nat. Rev. Clin. Oncol. *7*, 641–651. https://doi.org/10.1038/nrclinonc.2010.134.

25. Maurizi, A., and Rucci, N. (2018). The Osteoclast in Bone Metastasis: Player and Target. Cancers *10*. https://doi.org/10.3390/cancers10070218.

26. Le Pape, F., Vargas, G., and Clezardin, P. (2016). The role of osteoclasts in breast cancer bone metastasis. J Bone Oncol *5*, 93–95. https://doi.org/10.1016/j.jbo.2016.02.008.

27. Gnant, M., Pfeiler, G., Steger, G.G., Egle, D., Greil, R., Fitzal, F., Wette, V., Balic, M., Haslbauer, F., Melbinger-Zeinitzer, E., et al. (2019). Adjuvant denosumab in postmenopausal patients with hormone receptor-positive breast cancer (ABCSG-18): disease-free survival results from a randomised, double-blind, placebo-controlled, phase 3 trial. Lancet Oncol. *20*, 339–351. https://doi.org/10.1016/S1470-2045(18)30862-3.

28. Early Breast Cancer Trialists' Collaborative, G. (2015). Adjuvant bisphosphonate treatment in early breast cancer: meta-analyses of individual patient data from randomised trials. Lancet *386*, 1353–1361. https://doi.org/10.1016/S0140-6736(15)60908-4.

29. Drake, M.T., Clarke, B.L., and Khosla, S. (2008). Bisphosphonates: mechanism of action and role in clinical practice. Mayo Clin. Proc. *83*, 1032–1045. https://doi.org/10.4065/83.9.1032.

30. Russell, R.G. (2007). Bisphosphonates: mode of action and pharmacology. Pediatrics *119* (*Suppl 2*), S150–S162. https://doi.org/10.1542/peds.2006-2023H.

31. Sun, J., Lu, Q., Sanmamed, M.F., and Wang, J. (2021). Siglec-15 as an Emerging Target for Next-generation Cancer Immunotherapy. Clin. Cancer Res. *27*, 680–688. https://doi.org/10.1158/1078-0432.CCR-19-2925.

32. Jiang, K.Y., Qi, L.L., Kang, F.B., and Wang, L. (2022). The intriguing roles of Siglec family members in the tumor microenvironment. Biomark Res *10*, 22. https://doi.org/10.1186/s40364-022-00369-1.

33. Angata, T. (2020). Siglec-15: a potential regulator of osteoporosis, cancer, and infectious diseases. J. Biomed. Sci. *27*, 10. https://doi.org/10.1186/s12929-019-0610-1.

34. Ren, X. (2019). Immunosuppressive checkpoint Siglec-15: a vital new piece of the cancer immunotherapy jigsaw puzzle. Cancer Biol Med *16*, 205–210. https://doi.org/10.20892/j.issn.2095-3941.2018.0141.

35. Salerno, F., Freen-van Heeren, J.J., Guislain, A., Nicolet, B.P., and Wolkers, M.C. (2019). Costimulation through TLR2 Drives Polyfunctional CD8(+) T Cell Responses. J. Immunol. *202*, 714–723. https://doi.org/10.4049/jimmunol.1801026.

36. Mills, K.H. (2011). TLR-dependent T cell activation in autoimmunity. Nat. Rev. Immunol. *11*, 807–822. https://doi.org/10.1038/nri3095.

37. Wang, Y., Su, L., Morin, M.D., Jones, B.T., Mifune, Y., Shi, H., Wang, K.W., Zhan, X., Liu, A., Wang, J., et al. (2018). Adjuvant effect of the novel TLR1/TLR2 agonist Diprovocim synergizes with anti-PD-L1 to eliminate melanoma in mice. Proc. Natl. Acad. Sci. USA *115*, E8698–E8706. https://doi.org/10.1073/pnas.1809232115.

38. Hennessy, E.J., Parker, A.E., and O'Neill, L.A. (2010). Targeting Toll-like receptors: emerging therapeutics? Nat. Rev. Drug Discov. *9*, 293–307. https://doi.org/10.1038/nrd3203.

39. Pearce, O.M., and Laubli, H. (2016). Sialic acids in cancer biology and immunity. Glycobiology *26*, 111–128. https://doi.org/10.1093/glycob/cwv097.

40. Dobie, C., and Skropeta, D. (2021). Insights into the role of sialylation in cancer progression and metastasis. Br. J. Cancer *124*, 76–90. https://doi.org/10.1038/s41416-020-01126-7.

41. Pietrobono, S., and Stecca, B. (2021). Aberrant Sialylation in Cancer: Biomarker and Potential Target for Therapeutic Intervention? Cancers *13*. https://doi.org/10.3390/cancers13092014.

42. Kolbl, A.C., Andergassen, U., and Jeschke, U. (2015). The Role of Glycosylation in Breast Cancer Metastasis and Cancer Control. Front. Oncol. *5*, 219. https://doi.org/10.3389/fonc.2015.00219.

43. Ozturk, L.K., Emekli-Alturfan, E., Kasikci, E., Demir, G., and Yarat, A. (2011). Salivary total sialic acid levels increase in breast cancer patients: a preliminary study. Med. Chem. *7*, 443–447. https://doi.org/10.2174/157340611796799230.

44. Hogan-Ryan, A., Fennelly, J.J., Jones, M., Cantwell, B., and Duffy, M.J. (1980). Serum sialic acid and CEA concentrations in human breast cancer. Br. J. Cancer *41*, 587–592. https://doi.org/10.1038/bjc.1980.101.

45. Scott, D.A., and Drake, R.R. (2019). Glycosylation and its implications in breast cancer. Expert Rev. Proteomics *16*, 665–680. https://doi.org/10.1080/14789450.2019.1645604.

46. Lairson, L.L., Henrissat, B., Davies, G.J., and Withers, S.G. (2008). Glycosyltransferases: structures, functions, and mechanisms. Annu. Rev. Biochem. *77*, 521–555. https://doi.org/10.1146/annurev.biochem.76.061005.092322.

47. Zhou, X., Zhai, Y., Liu, C., Yang, G., Guo, J., Li, G., Sun, C., Qi, X., Li, X., and Guan, F. (2020). Sialidase NEU1 suppresses progression of human bladder cancer cells by inhibiting fibronectin-integrin alpha5beta1 interaction and Akt signaling pathway. Cell Commun. Signal. *18*, 44. https://doi.org/10.1186/s12964-019-0500-x.

48. Muhsin-Sharafaldine, M.R., and McLellan, A.D. (2018). Tumor-Derived Apoptotic Vesicles: With Death They Do Part. Front. Immunol. *9*, 957. https://doi.org/10.3389/fimmu.2018.00957.

49. Lynch, C., Panagopoulou, M., and Gregory, C.D. (2017). Extracellular Vesicles Arising from Apoptotic Cells in Tumors: Roles in Cancer Pathogenesis and Potential Clinical Applications. Front. Immunol. *8*, 1174. https://doi.org/10.3389/fimmu.2017.01174.

50. Pavlyukov, M.S., Yu, H., Bastola, S., Minata, M., Shender, V.O., Lee, Y., Zhang, S., Wang, J., Komarova, S., Wang, J., et al. (2018). Apoptotic Cell-Derived Extracellular Vesicles Promote Malignancy of Glioblastoma Via Intercellular Transfer of Splicing Factors. Cancer Cell *34*, 119–135. https://doi.org/10.1016/j.ccell.2018.05.012.

STAR★METHODS

KEY RESOURCES TABLE

REAGENT or RESOURCE	SOURCE	IDENTIFIER
Antibodies		
Rabbit anti-Histone 3	Bioss	Cat#bs-17422R
Rabbit anti-C1QC	Bioss	Cat#bs-11336R
Rabbit anti-H2B	Bioss	Cat#bs-52009R
Rabbit anti-C3B	Bioss	Cat#bs-4871R
Rabbit anti-GAPDH	Bioss	Cat#bs-2188R;RRID:AB_10856675
Rabbit anti-β-tubulin	Bioss	Cat#bs-0715R;RRID:AB_10853042
Rabbit anti-CD8	Bioss	Cat#bs-4790R
Rabbit anti-Granzyme B	Bioss	Cat#bs-1351R;RRID:AB_10856802
Rabbit anti-IRAK4	Bioss	Cat#bs-2440R;RRID:AB_11067218
Rabbit anti-TRAF6	Bioss	Cat#bs-2830R
Rabbit anti-TAK1	Bioss	Cat#bs-3585R;RRID:AB_10855725
Rabbit anti-Siglec15	KleanAB	Cat#P103014
Anti-mouse RANK-PE	Biolegend	Cat#119805;RRID: AB_2205354
Anti-mouse CD3e	eBioscience	Cat#16-0033-86;RRID:AB_842782
Anti-rabbit IgG, HRP-linked Antibody	Cell Signaling Technology	Cat#7074;RRID:AB_2099233
Bacterial and virus strains		
Lentivirus-luc-gfp-puro	HanBio https://www.hanbio.cn/cn/services/item/1	N/A
Biological samples		
Human Primary $CD8^+$ T cells	MEISEN CELL	Cat#CTCC-009-287
Chemicals, peptides, and recombinant proteins		
Biotin MAL-II	Vector Laboratories	Cat#B-1265-1
Biotin SNA	Vector Laboratories	Cat#B-1305-2
FITC-Streptavidin	Biolegend	Cat#405201
Recombinant mouse RANKL	R&D Systems	Cat#462-TR-010
Recombinant mouse M-CSF	R&D Systems	Cat#416-ML-050
Recombinant mouse Siglec15	R&D Systems	Cat#5A4074-M31H
Staurosporine	MedChemExpress	Cat#HY-15141
Microspheres	Aladdin	Cat#M122073/M122077
Alendronate sodium	Aladdin	Cat#A115345
Sialidase	Sigma-Aldrich	Cat#11585886001
D-luciferin salt solution	Meilunbio	Cat#MB1834-2
5,6-carboxyfluorescein diacetate succinimidyl ester	Thermo Scientific	Cat#C34570
6′-sialic acid lactose sodium salt	MACKLIN	Cat#S868592
Critical commercial assays		
TRAP stain kit	Sigma-Aldrich	Cat#CS0740
Annexin V and PI Apoptosis Kit	US Everbright	Cat#F6012
EasySep Mouse Naive $CD8^+$ T cell Isolation Kit	StemCell Technologies	Cat#19858
Cell Counting Kit-8	Beyotime Biotechnology	Cat#C0038
Mouse IFN-γ Elisa Kit	FankeW	Cat#F2182-A
Mouse TNF-α Elisa Kit	FankeW	Cat#F2132-A
Mouse IL-2 Elisa Kit	FankeW	Cat#F2698-A

(*Continued on next page*)

Continued

REAGENT or RESOURCE	SOURCE	IDENTIFIER
Human IFN-γ Elisa Kit	4A Biotech	Cat#CHE0017
RNA-Quick Purification Kit	YiShanBiotech	Cat#ES-RN001
BCA protein assay Kit	Beyotime Biotechnology	Cat#P0010
DAB Chromogenic Kit	Beyotime Biotechnology	Cat#P0203
Mouse Spleen Lymphocyte Isolation Kit	Solarbio	Cat#P8860
IHC Detection Reagent	Cell Signaling Technology	Cat#8114
TSA Fluorescent Triple Staining Kit	Servicebio	Cat# G1236
Deposited data		
Raw data and processed bulk RNA-seq data(mouse)	GEO	GEO:GSE133515/GSE132230
Siglec15-interacting proteins	ProteomeXchange Consortium	PXD:006359
Experimental models: Cell lines		
4T-1	Procell	Cat #CL-0007
EMT-6	Procell	Cat #CL-0573
THP-1	Procell	Cat#CL-0233
HEK293	Procell	Cat#CL-0005
MA-891	iCellBioscience	Cat#iCell-m029
Experimental models: Organisms/strains		
Mouse: C57BL/6J	Laboratory Animal Center of Third Military Medical University	N/A
Mouse: BALB/c	Laboratory Animal Center of Third Military Medical University	N/A
Mouse: MRL/lpr	The Jackson Laboratory	JAX:000485
Mouse:Siglec15$^{-/-}$	SHANGHAI MODEL ORGANISMS	NM-KO-191192
Oligonucleotides		
Siglec15 primer forward 5′-CAGCACCGAGATGTTGACGA-3′	TsingkeBiotechnology	N/A
Siglec15 primer reverse 5′-ACGATCGCTATGAGAGTCGC-3’.	TsingkeBiotechnology	N/A
GAPDH primer forward 5′-AACGGTCGGAACGATAGCA-3’;	TsingkeBiotechnology	N/A
GAPDH primer forward 5′-CCTTAAGGCGTAGTTAGGCCC-3’.	TsingkeBiotechnology	N/A
Software and algorithms		
FlowJo V10	FlowJo	https://www.flowjo.com/
Prism 8.0	GraphPad	https://www.graphpad.com/
ImageJ v1.8.0	ImageJ	https://imagej.net/
Image Lab	Image Lab	www.bio-rad.com
ANIVIEW100	ANIVIEW100	https://www.bltlux.com/
CTvox v3.3.0	CTvox	https://www.bruker.com/en/products-and-solutions/diffractometers-and-x-ray-microscopes/3d-x-ray-microscopes/xrm-software.html
DataViewer v1.5.6.2	DataViewer	https://www.bruker.com/en/products-and-solutions/diffractometers-and-x-ray-microscopes/3d-x-ray-microscopes/xrm-software.html
CTAN v1.20.3.0	CTAN	https://www.bruker.com/en/products-and-solutions/diffractometers-and-x-ray-microscopes/3d-x-ray-microscopes/xrm-software.html

RESOURCE AVAILABILITY

Lead contact

Further information and requests for resources and reagents should be directed to and will be fulfilled by the lead contact, Ce Dou (lance.douce@gmail.com).

Materials availability

This study did not generate new unique reagents.

Data and code availability

- Data: RNA-Seq data have been deposited at Gene Expression Omnibus (GEO: GSE133515, GSE132230) and is publicly available. This paper analyzes existing, publicly available data (Proteo-meXchange Consortium, PXD006359). Microscopy data reported in this paper will be shared by the lead contact upon request.
- Code: This paper does not report original code.
- Any additional information required to reanalyze the data reported in this paper is available from the lead contact upon request.

EXPERIMENTAL MODEL AND SUBJECT DETAILS

In vivo animal studies

C57BL/6J, BALB/c, MRL/lpr and Siglec15$^{-/-}$ female mice were bred and housed at Laboratory Animal Center of Third Military Medical University (Chongqing, China). All experimental protocols were reviewed and approved by the Institutional Animal Care and Use Committee of Third Military Medical University. All mice were maintained under 12-h light, 12-h dark cycles and free to food and water, and the mice were euthanized according to the AVMA Guidelines for the Euthanasia of Animals.

Cell lines and primary cultures

Mouse breast cancer 4T-1 cell line, EMT-6 cell line and MA-891 cell line were cultured with Dulbecco's Modified Eagle Medium (DMEM; Procell, Wuhan, China) containing 10% fetal bovine serum (FBS; CELLCOOK, Guangzhou, China) and 1% penicillin-streptomycin. HEK293 cell line was cultured with DMEM containing 10% FBS and 1% penicillin-streptomycin. Mouse and human primary CD8$^+$ T cells were cultured with Roswell Park Memorial Institute 1640 (RPMI-1640; Procell, Wuhan, China) containing 10% FBS; and 1% penicillin-streptomycin. Mouse primary marrow mononuclear cells were cultured with DMEM containing 10% FBS, 1% penicillin-streptomycin and 50 ng/mL M-CSF. Human monocyte THP-1 cell line was cultured with RPMI-1640 containing 10% FBS; and 1% penicillin-streptomycin.

METHOD DETAILS

Cell counting Kit-8 test

After inoculating equal amounts of cells in 96-well plates, different cell-derived ABS (1:30 ratio of cells to ABS) were added to the media of each group according to the experimental design. 10 μL CCK-8 solution was added into each well after the culture system was stabilized. 100 μL basal medium was added with 10 μL CCK-8 solution as blank control. The absorbance was determined at 450 nm after incubation for 1 h in the cell incubator.

Induction of osteoclastogenesis and apoptosis

Primary cultured bone marrow mononuclear cells (BMMs) were used to mimic osteoclast differentiation *in vivo*. Mouse bone marrow cells were isolated from 11-week old male C57BL/6 mouse hind limbs (femur and tibia) and incubated with M-CSF (50 ng/mL) for 96 h to obtain BMMs. BMMs were cultured with DMEM containing 10% FBS, 1% PG-S, 30 ng/mL M-CSF and 50 ng/mL RANKL for obtaining osteoclasts. After 120 h osteoclastogenesis, medium of osteoclasts was changed to DMEM containing 5 μM STS and continue incubating for 4 h to promote osteoclasts apoptosis.

Apoptotic body extraction and identification

Osteoclasts were treated with STS for 4 h and then the supernatant was collected for a sequential centrifugation. We chose 300 × g centrifugation for 10 min to remove cell debris and 3000 × g for 30 min to pellet the apoptotic body-sized extracellular vesicles according to Minimal Information 2018 for Studies of Extracellular Vesicles (MISEV2018) guidelines. The pellet apoptotic body were resuspended in 5 mL PBS and the centrifuged again at 3000 × g for 30 min. All centrifugation operations were performed at 4°C using Optima XE-90 (Beckman Coulter). To observe apoptotic bodies, the pelleted AB was incubated with Annexin-V/FITC for 15 min in the dark, centrifuged at 3000 × g, resuspended in 100 μL PBS, and dropped on a glass slide for observation by Zeiss LSM-800 microscope. The size distribution and concentration of separated ABs was examined using a ZataView (Particle 140 Metrix, Germany). Further, 10 μL 1μm-sized microspheres (#*M122073*, Aladdin, Shanghai, China) and 10 μL 5μm-sized microspheres (#*M122077*,

Aladdin, Shanghai, China) were added to 500 μL apoptotic body suspension for detecting the purity of the extracted apoptotic bodies by flow analysis. C1QC, C3B, H3 and H2B were used to assess the purity of OC-ABs by Western blot.

Establishment of breast cancer bone metastases mouse model and treatment

The 8-week-old female mice in each experimental group were implanted with breast cancer cells in the bilateral tibia to establish the femoral metastasis model. Briefly, 1×10^6 luciferase-transfected 4T-1 cells were resuspended in 100 μL of PBS, and an insulin needle was used to penetrate the tibia plateau and slowly injected the tumor suspension into per bone marrow cavity. A week later detection of modeling results by bioluminescence imaging. Breast cancer mice with bone metastases were intraperitoneally injected with alendronate sodium (2 mg/kg, dissolved in PBS), Siglec15 neutralizing antibody (200 μg/mice, dissolved in PBS), and intratumoral injection of sialidase (0.2 U, dissolved in PBS); Alendronate sodium was purchased from Aladdin (Shanghai, China). sialidase was purchased from Sigma-Aldrich (Shanghai, China). Siglec15 neutralizing antibody was produced by Sino Biological Inc (Beijing, China). Isotype antibody shares the same heavy chain IgG1 as the S15 NAB was used as control with no significant difference relative to PBS as a general control. Though intracardiac injection is a well-accepted model, it is not the best option in the study of bone-centered further disseminations. The setbacks include: Introduction of non-bone metastases that often shorten animal survival; High experimental variability; incapable of delineating further metastasis from bone.

Bioluminescence imaging

200 μL of D-luciferin salt solution (#*MB1834-2*, Meilunbio, Dalian, China) with 200 mg/kg working concentration was injected intraperitoneal into mice 5 min before imaging. 4% mixture of isoflurane (Pathology laboratory, Southwest Hospital, China) in oxygen was used for introductory anesthesia and 2% mixture for maintenance anesthesia. AniView100 Intravital Fluorescence Imaging System (BioLight, Guangzhou, China) was used to detect the fluorescence intensity and range of tumor. The AniView BLT software (BioLight, Guangzhou, China) was used to quantify the area of the tumor. Tumor size and metastases area were detected and recorded weekly for analyze.

Generation of Siglec15 neutralizing antibodies

The gene of Siglec15 antibody was amplified by PCR and inserted into the corresponding expression vector. The sequence of the constructed vector was verified by sequencing and the correct plasmid was amplified. Subsequently, the plasmids were mixed with transfection reagents and added into the flask containing HEK293. The mixed system was cultured in a serum-free medium and maintained in Erlenmeyer Flasks on an orbital shaker by a suitable stirring speed at 37°C for 6 days. The cell supernatant was then collected and loaded onto the affinity purification column at the appropriate flow rate. Finally, SDS-PAGE and endotoxin analysis were performed on the purified protein, and the qualified antibody preparations were lyophilized for long-term storage.

Immunohistochemistry and immunofluorescence staining

Mouse tibia with surrounding tumor tissue and lung tissue were collected 2 or 4 weeks after the establishment of the breast cancer bone metastasis model. The samples with bone tissue were infiltrated and fixed with 4% paraformaldehyde for 1 week and then entered the decalcification stage, and the EDTA decalcification solution was renewed every two days. After the bone tissue was completely softened, it was dehydrated and embedded in paraffin, and a Leica microtome (RM2235, Leica Biosystems, Germany) was used to make 5 μm thick sections for subsequent IHC staining. The decalcification step for lung tissue was omitted and 5 μm thick sections were made for H&E staining. For IHC, the expression of CD8, Granzyme B, IRAK4, TRAF6 and TAK1 were detected according to the following procedure. First, the sections were dewaxed in a gradient manner, and 3% H_2O_2 was added dropwise for 15 min to block, and then the sections were immersed in sodium citrate antigen retrieval solution for 10 min at 95°C. After cooling down, sections were incubated with 5% blocking solution (Beyotime Biotechnology, Shanghai, China) for 15 min, followed by rabbit anti-CD8, anti-Granzyme B, anti-IRAK4, anti-TRAF6 and anti-TAK1 (1:200, diluted in 5% blocking solution) for 2 h at 37°C, respectively. After three time wash in PBS, sections were incubated with horseradish peroxidase-conjugated secondary antibody for 2 h. After three time wash in PBS, sections were chromogenic stained by a DBA Chromogenic Kit (Beyotime Biotechnology, Shanghai, China) and observed using light microscopy. Double-blind readings were performed by two experienced pathologists, and scoring by using the German semi-quantitative method.

$CD8^+$ T cell sorting and proliferation assay

The spleen from 8-week-old mouse was harvested under sterile conditions, the spleen capsule was torn off, and the spleen was cut into small pieces with ophthalmic scissors. The spleen was then grounded and passed through a 200-mesh cell filter to prepare a single-cell suspension. Subsequently, spleen lymphocytes were extracted and purified by using the mouse spleen lymphocyte isolation solution kit (Solarbio, Beijing, China) according to the manufacturers' instructions. After purification, naive $CD8^+$ T cells were isolated using the Mouse Naive $CD8^+$ T cell Isolation Kit (#*19858*, EasySep, Stemcell, Canada). To activate and proliferate naive $CD8^+$ T cells, the naive $CD8^+$ T cells were seeded into cell plates which were pre-coat by anti-CD3e antibody. Naive $CD8^+$ T cells in some experiments need to be stained with 5,6-carboxyfluorescein diacetate succinimidyl ester (CFSE, CellTrace, Thermo Scientific, MA, USA) in advance. After stimulation with different experimental conditions, CytoFLEX flow cytometer (Beckman, California, USA) was used to quantify the proliferation of $CD8^+$ T cells.

Enzyme-linked immunosorbent (ELISA) assay

Tumor necrosis factor alpha (TNF-α), interferon gamma (IFN-γ), interleukin-2 (IL-2) were measured with ELISA kits purchased from FankeW (Shanghai, China) according to the manufacturers' instructions. BioTek Synergy HT Multifunctional Microplate Assay System (BioTek, Vermont, USA) was used to quantitative absorbance value at 450 nm.

Multiple fluorescence staining

5 μm thick sections of tumor tissue were prepared for multiple immunofluorescence staining. First, sections were dewaxed in a gradient fashion, blocked by 3% H_2O_2 dripping for 15 min, and then the sections were immersed in Sodium Citrate antigen retrieval solution at 95°C for 10 min. After cooling, sections were incubated with 5% blocking solution for 15 min before CD8 antibody (1:100, diluted in 5% blocking solution) was added to cover the tissue, the slices were placed in a wet box with water at 4°C and incubated overnight. After three washes in PBS, sections were incubated with HRP-secondary antibodies for 50 min at room temperature. After three washes in PBS, 50 μL TSA-488 staining solution was dripped onto the tissue to ensure complete coverage of the tissue, and the tissue was incubated at room temperature for 10 min without light. The antigen retrieval step was repeated after 3 washes in PBS, and then GZMB antibodies (1:100, diluted in 5% blocking solution) were added to the sections and incubation of secondary antibodies was completed, after that, 50 μL TSA-555 staining solution was added to cover the tissues and incubated for 10 min at room temperature without light. The same steps were repeated after 3 PBS washes, completing incubation with siglec15 antibody (1:100, diluted in 5% blocking solution), and 50 μL TSA-647 staining solution addition steps. Finally, Dapi staining solution was added to the tissue sections and the nuclei were stained after 10 min incubation in dark room. The data were analyzed in a single-blind manner, using ImageJ to quantify the fluorescence intensity.

Micro-CT

Images of the femur were acquired using a Bruker MicroCT Skyscan 1272 system (Kontich, Belgium) with a resolution of 8.0 μm voxel size and data reconstruction was performed using Nrecon (Kontich, Belgium). Select regions of interest (ROIs) and acquire 2D images in DataViewer 1.5.6.2 (Bruker, Kontich, Belgium). The bone volume fraction and other data of the ROI were obtained by CTAn 1.20.8.0 (Bruker, Kontich, Belgium) software.

Real-time PCR (PCR)

Total RNA was isolated from the cultures using the RNA-Quick Purification Kit (YiShanBiotech, Shanghai, China) according to the manufacturer's instructions. The cDNA was synthesized using SuperScript III (Life Technologies). The real-time PCR was performed using SYBR Green Supermix (Toyobo) and gene-specific primers. The primers included *Siglec15* forward 5′-CAGCACCGAGATGTT GACGA-3'; reverse 5′-ACGATCGCTATGAGAGTCGC-3'. *GAPDH* forward 5′-AACGGTCGGAACGATAGCA-3'; 5′CCTTAAGGCGTA GTTAGGCCC-3'. *GAPDH* was used as an endogenous control for osteoclasts. Real-time PCR was detected on a CFX96 Real-Time PCR System (Bio-Rad).

Western blot analysis and co-immunoprecipitation analysis

Cells or ABs were lysed in RIPA lysis buffer (CWBIO, Beijing, China) mixing with protease phosphatase inhibitor (Beyotime Biotechnology, Shanghai, China). The lysis system was centrifuged at 12,000 × g for 15 min to obtain the supernatant after incubated on ice for 30 min. The BCA protein assay kit (Beyotime Biotechnology, Jiangsu, China) was used to detect the concentration of proteins. 50 μg protein samples were diluted in loading buffer (Beyotime Biotechnology, Jiangsu, China) and electrophoresed, followed by transferred onto polyvinylidene fluoride membranes (ImmobilonTM-PSQ Membranes, Sigma-Aldrich, China). and blocking in 5% skim milk. Protein on membranes were incubated with anti-IRAK4, anti-TRAF6 and anti-TAK1 (1:1000, diluted in 5% skim milk) antibodies for 12 h at 4°C. After washing in Tris-Buffered Saline Tween buffer three times, secondary antibodies linked HRP (1:10000, diluted in 5% skim milk) against primary antibodies were used to incubate membranes. Super ECL Plus (Biosharp, Anhui, China) and Immun-Star HRP (BioRad) were used to detect chemiluminescent signals. Super ECL Plus (Bioground, Chongqin, China) and the ChemiDoc XRS+ gel imaging system (BioRad) were used to detect chemiluminescent signals.

RNA-seq

RNA-seq was used to screen the gene expression profile of the mouse *siglec* family, which was deposited at Gene Expression Omnibus (GEO: GSE133515). Briefly, after first isolating total RNA from different stages of osteoclast differentiation, transcripts are fragmented and converted to cDNA under conditions that meet quality and purity requirements. cDNA is used for library creation and subsequently sequenced on Illumina NovaSeq 6000 platform.

QUANTIFICATION AND STATISTICAL ANALYSIS

All experiments were repeated at least three times carried out with at least three biological replicates. Comparisons between two groups were analyzed by using independent unpaired two-tailed Student's t-tests and Mantel-Cox test for survival analysis. Prism 8.0 software (GraphPad) was used for statistical analysis. p values <0.05 and p values <0.01 were used to represent the significance of the difference. The error bars in the figures represent the standard deviation (SD).